

EXERGY-BASED AERODYNAMIC CHARACTERISTICS ANALYSIS OF THE NASA COMMON RESEARCH MODEL AND BWB CONFIGURATION CIVIL AIRCRAFT

Huicheng Yang[1], Xukang Ma[1], Rongbo Zhu[1], Kai You[1] & Zhenli Chen[1,2]

[1]School of Aeronautics, Northwestern Polytechnical University, Xi'an 710072, China
[2]National Key Laboratory of Aircraft Configuration Design, Xi'an 710072, China

Abstract

For transonic civil aircraft, the complex physical origins of drag pose challenges in clearly identifying drag sources and implementing effective drag reduction strategies during the design phase. An analysis method based on the exergy transport offers a clear characterization of drag sources and their streamwise conversion mechanisms. By linking the contributions of various exergy terms in the flow field to specific physical phenomena, this method provides deeper insights into the loss mechanisms that degrade system performance. In this study, the exergy-based method is applied to analyze the NASA Common Research Model and a Blended-Wing-Body (BWB) civil aircraft configuration. The predicted drag is compared with results obtained using the near-field and far-field methods, showing minimum and maximum deviations of 0.06% and 1%, respectively. Finally, a quantitative analysis of exergy outflows and anergy generation is conducted to clarify the origins of different drag components and their underlying physical conversion mechanisms.

Keywords: exergy, anergy, drag components, physical conversion mechanisms

1. Introduction

Since the first commercial flight, the air transportation industry has experienced remarkable growth. According to forecasts by both Airbus and Boeing, more than 43,000 new aircraft will be required between 2025 and 2044 to meet rising market demand[1][2]. This expansion raises environmental concerns, creating a dual objective: enhancing performance while reducing fuel consumption and emissions.

Even with continued improvements, the conventional tube-and-wing configuration may struggle to meet these emerging constraints. A highly promising alternative is the blended-wing-body (BWB) layout[3][4]. To accurately assess the aerodynamic performance benefits of such novel configurations, advanced drag prediction methods are essential.

The drag of a transonic transport aircraft comprises profile drag, induced drag, wave drag, and interference drag. Several computational fluid dynamics (CFD) approaches are available for drag prediction. The conventional near-field method calculates drag by integrating pressure and shear stresses over the aircraft surface, but it can only decompose drag into pressure drag and friction drag. In contrast, the far-field method, based on the momentum theorem, links drag generation to entropy and momentum changes. This method enables drag decomposition according to physical origins, such as viscous drag, wave drag, and induced drag. However, the far-field method only evaluates the mechanical energy performance of the flow and neglects thermal energy[5][7]. Recently, Wu et al.[8] related aerodynamic forces to the vorticity field, providing physical insight into drag generation[9]. In their formulation, the force exerted on a body can be fully determined by integrals over a control surface enclosing the body, involving vorticity and velocity, without requiring volume integration. This approach provides a theoretical foundation for flow-diagnostics-based drag prediction.

Subsequently, the power balance method proposed by Drela[10] enables the analysis of novel configurations such as the BWB from a mechanical energy perspective, and its physical interpretation has been further explored[11]. However, this method also neglects thermal effects. More recently, Arntz[12][13] proposed an approach based on exergy, which accounts for thermal energy in addition to mechanical energy. By integrating the first and second laws of thermodynamics, exergy analysis allows any form of energy to be divided into two parts: the part that can theoretically be completely converted into mechanical work, and the part that cannot. Following the terminology of Ran[14], these two parts are referred to as exergy and anergy, respectively. Since exergy represents the economically valuable portion of energy[15], it requires careful management.

In recent decades, exergy analysis has attracted growing interest in the field of aerospace engineering. Moorhouse and Camberos, for example, introduced exergy analysis into aircraft design[16][17]. Arntz et al. developed an exergy balance equation suitable for external aerodynamic analysis[12][18], which links different components of exergy to reversible and irreversible physical phenomena. Over the past several years, this exergy-based method has been successfully applied to both conventional and disruptive aircraft configurations[18] and has been further refined numerically[19]. More recently, it has also been extended to various numerical and experimental scenarios[20][22].

The exergy definition proposed by Arntz et al., suffers from a drawback that positive exergy cannot be guaranteed. Berhouni et al. [23] clarified a conceptual distinction between “exergy” and “flow exergy.” They derived an unsteady exergy balance equation in the geocentric reference frame, in which the definition of exergy is unambiguous and positive. By subsequently transforming this exergy definition into a reference frame fixed to the aircraft, they obtained a formulation that resolves the non-negativity issue, thereby addressing a previous shortcoming in aerodynamic exergy analysis. Later, the exergy balance equation was extended to rotating reference frames[24]. Furthermore, Petropoulos et al. [25] addressed the discrete-error problem in the far-field exergy balance method within numerical simulations. They developed a dedicated set of numerical accuracy metrics, which was validated using the NACA 0012 airfoil and the NASA Common Research Model (CRM). Their results demonstrated that these metrics can effectively identify error sources, providing a quantitative assessment tool for ensuring the accuracy of exergy balance analyses.

In the present work, the near-field, far-field, and exergy-based drag prediction methods are compared through post-processing of CFD simulations of the CRM and BWB aircraft. This comparison aims to validate the exergy-based method and to highlight the differences in drag components between the CRM and BWB configurations. Furthermore, the streamwise conversion of drag is analyzed to clarify the origins of drag and the associated physical transfer mechanisms. The recoverable exergy is also quantified to provide physical insight for the design of BWB aircraft.

2. Drag-prediction Methods

2.1 Near-Field and Far-Field Drag-Prediction Methods

The drag experienced by an unpowered configuration has historically been determined using a force balance.

The most direct approach to evaluate the drag acting on an object is to directly integrate the surface stresses, thereby decomposing the drag into a pressure drag D_p and a friction drag D_f as shown in Equations (1)-(3):

$$D_{nf} \coloneqq D_p + D_f , \tag{1}$$

$$D_p = \int_{S_b} P_s \boldsymbol{n} dS_b , \tag{2}$$

$$D_f = \int_{S_b} \bar{\bar{\tau}} \cdot \boldsymbol{n} dS_b , \tag{3}$$

where P_s is the static pressure. $\bar{\bar{\tau}}$ is the viscous stress tensor. $\boldsymbol{n}$ is the normal vector of the body.

S_b is the body surface area.

Numerically speaking, the approach is unambiguous and straightforward, but it highly depends on mesh. Therefore, it suffers from insufficient accuracy on the coarse meshes.

Far-field drag methods are diverse in type, with origins traceable to Betz[26], who proposed calculating drag by analyzing the rate of momentum change across a surface downstream of the body. As the surface is usually located within a few body lengths downstream of the geometry, or even less, the methods are actually not too far field. In the study, the methods proposed by Meheut[27] and Kusunose[28] are used as the second benchmark for comparison. The Meheut method combines small-disturbance theory with axial velocity deficit decomposition and is applicable to both compressible and incompressible flow fields, with third-order errors. It provides the most accurate profile drag value among all far-field methods and has the additional advantage of reducing the measurement region to the wake zone. However, its limitation lies in that the measurement plane cannot be placed within one chord length from the body. In most cases, both viscous drag and wave drag coexist in the flow field. The above profile drag formula cannot distinguish between wave drag and viscous drag. To achieve their separation, it is necessary to first calculate the profile drag and then apply the physical reasoning method proposed by Kusunose, dividing the profile drag measurement region into a shock wave zone and a viscous zone. Through the above far-field method, drag can be decomposed into viscous drag D_v, induced drag D_i, and wave drag D_w:

$$D_{ff} := D_v + D_i + D_w, \tag{4}$$

$$D_p = D_v + D_w, \tag{5}$$

$$D_p = \frac{\rho_0 {u_0}^2}{2}\int_{S_{wake}}[-\frac{2}{\gamma {M_0}^2}\Delta P_t - \Delta T_t + (1-\frac{{M_0}^2}{4})\Delta T_t^2 - \Delta P_t \Delta T_t - (1-{M_0}^2)(\Delta\bar{u}^2 + 2\Delta u^*\Delta\bar{u})]dS. \tag{6}$$

With:

$$\Delta P_t = \frac{P_t}{P_{t_0}} - 1, \tag{7}$$

$$\Delta T_t = \frac{T_t}{T_{t_0}} - 1, \tag{8}$$

$$\Delta u = \frac{u}{U_0} - 1, \tag{9}$$

$$\Delta u^* = \sqrt{1 - \frac{2}{(\gamma-1){M_0}^2}\left(\left(\frac{P_s}{P_{s_0}}\right)^{\frac{(\gamma-1)}{\gamma}} - 1\right) - \frac{v^2+w^2}{{U_0}^2} - 1}, \tag{10}$$

$$\Delta\bar{u} = \Delta u - \Delta u^*, \tag{11}$$

$$D_i = \int_{S_{wake}} \frac{\rho_0}{2}\psi\xi dS = \int_{S_{out}} \frac{\rho_0}{2}\left[\left(v^2+w^2\right) - \left(1-M_0^2\right)\delta u^2\right]dS, \tag{12}$$

where ρ_0 is the freestream gas density. u_0 is the freestream axial velocity. γ is ratio of specific heats. M_0 is the freestream Mach number. P_t is the local total pressure measured in the wake. P_{t_0} is the freestream total pressure. T_t and T_{t_0} are the local and freestream total temperatures. u is the local streamwise velocity. U_0 is the freestream velocity. P_s and P_{s_0} are the local and freestream static pressures. v and w are the transverse velocity components. $\Delta\bar{u}$ represents the mean streamwise velocity deficit. Δu^* is a characteristic quantity of the turbulent fluctuating velocity. δu^2 is the squared streamwise fluctuating velocity.

The far-field method defines the viscous and shock wave components based on physical criteria. The

approach has the advantage of providing a physical breakdown of drag.

2.2 Exergy-Based Method

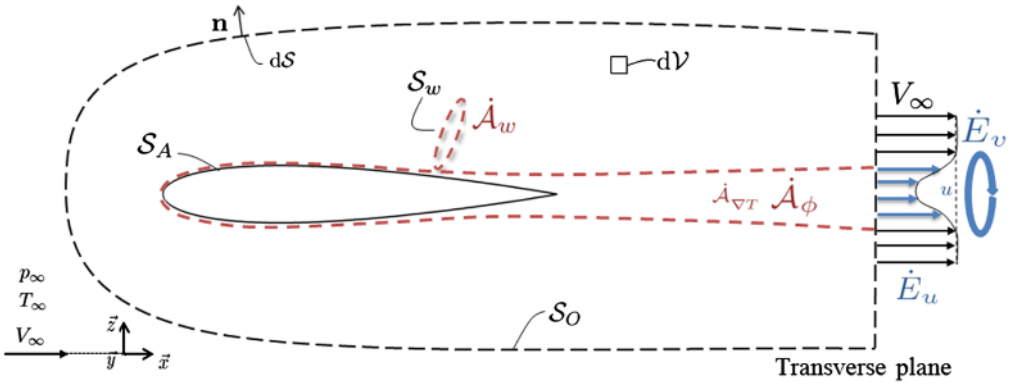


Figure 1-A sketch of the exergy balance in the flowfield.[12]

The exergy method employed in the paper is applicable to steady flows without thermal or mechanical energy input. The analysis focuses on a continuous control volume surrounding the target object, as illustrated in Figure 1. The volume is bounded by the aircraft surface $\mathcal{S}_A$, a surface $\mathcal{S}_w$ that excludes all discontinuous shock waves, and the outer boundary $\mathcal{S}_O$. The selection of the outer boundary must satisfy the conditions that the upstream and lateral surfaces are far from the object, while the downstream surface is a fixed transverse plane perpendicular to the freestream.

Exergy is a thermodynamic property describing the maximum theoretical work that can be obtained from a substance in taking it from a given temperature and pressure/velocity to a state of thermal and mechanical equilibrium with the environment. We can say

$$Energy = Exergy + Anergy \Leftrightarrow Total = Useful + Useless\,, \tag{13}$$

which can be translated mathematically for an open system as

$$\varepsilon = \left(h_i - h_{i,\infty}\right) - T_\infty\left(s - s_\infty\right) = \delta h_i - T_\infty \delta s\,, \tag{14}$$

where ε is mass specific flow exergy. h_i is the local stagnation enthalpy in the wake. $h_{i,\infty}$ is the freestream stagnation enthalpy. T_∞ is the freestream static temperature. s is the local specific entropy in the wake, and s_∞ is the freestream specific entropy.

First, the total enthalpy is defined as the sum of the internal energy, the flow energy, and the kinetic energy, and its rate of change can therefore be written as

$$\nabla\cdot\left(\rho\delta h_i \boldsymbol{V}\right) = \nabla\cdot\left(\rho\delta e\boldsymbol{V}\right) + p_\infty\nabla\cdot\boldsymbol{V} + \nabla\cdot\left(p - p_\infty\right)\boldsymbol{V} + \nabla\cdot\left(\rho\frac{V^2}{2}\boldsymbol{V}\right), \tag{15}$$

where we have added and subtracted $p_\infty\nabla\cdot\boldsymbol{V}$ for further purposes. ρ is the local density. $\boldsymbol{V}$ is the local velocity vector.

Second, according to the first law of thermodynamics, the steady state Reynolds-averaged total enthalpy equation is as follows:

$$\nabla\cdot\left(\rho\delta h_i\boldsymbol{V}\right) = \nabla\cdot\left(\overline{\overline{\tau}}\cdot\boldsymbol{V}\right) - \nabla\cdot\boldsymbol{q}\,, \tag{16}$$

where $\boldsymbol{q}$ is the heat flux by conduction.

The Gibbs relation provides a relation between entropy and internal energy. In time-averaged form, it reads

$$T\nabla s = \nabla e + p\nabla\frac{1}{\rho}\,, \tag{17}$$

where e is the specific internal energy.

Inserting the steady-state expression of the internal energy variation:

$$\nabla\cdot\left(\rho\delta e\boldsymbol{V}\right)=-p\nabla\cdot\boldsymbol{V}+\left(\overline{\overline{\tau}}\cdot\nabla\right)\cdot\boldsymbol{V}-\nabla\cdot\boldsymbol{q}\,, \tag{18}$$

into the Equation (17) yields the following entropy relation:

$$\nabla\cdot\left(\rho\delta s\boldsymbol{V}\right)=\frac{1}{T}\left(\overline{\overline{\tau}}\cdot\nabla\right)\cdot\boldsymbol{V}-\frac{1}{T}\nabla\cdot\boldsymbol{q}\,. \tag{19}$$

Substituting Equation (16) (19) into Equation (14) yields

$$\nabla\cdot\left(\rho\varepsilon\boldsymbol{V}\right)=\nabla\cdot\left(\rho\delta h_i\boldsymbol{V}\right)-T_\infty\nabla\cdot\left(\rho\delta s\boldsymbol{V}\right). \tag{20}$$

Integrating the equation within the control volume before invoking the mass and momentum conservation as well as the first and second law of thermodynamics, one obtains the following drag-power relation:

$$DV_\infty=\dot{\varepsilon}_m+\dot{\varepsilon}_{th}+\dot{\mathcal{A}}_\phi+\dot{\mathcal{A}}_{\nabla T}+\dot{\mathcal{A}}_w\,. \tag{21}$$

The following explanations of each term correspond to Figure 1.

The mechanical exergy outflow:

$$\dot{\varepsilon}_m=\underbrace{\int_{\mathcal{S}_O}\frac{1}{2}\rho u^2\left(\boldsymbol{V}\cdot\boldsymbol{n}\right)\mathrm{d}\mathcal{S}}_{\dot{E}_u}+\underbrace{\int_{\mathcal{S}_O}\frac{1}{2}\rho\left(\upsilon^2+\omega^2\right)\left(\boldsymbol{V}\cdot\boldsymbol{n}\right)\mathrm{d}\mathcal{S}}_{\dot{E}_v}+\underbrace{\int_{\mathcal{S}_O}(p-p_\infty)\left[\left(\boldsymbol{V}-\boldsymbol{V}_\infty\right)\cdot\boldsymbol{n}\right]\mathrm{d}\mathcal{S}}_{\dot{E}_p}\,, \tag{22}$$

$\dot{E}_u$ is the streamwise kinetic energy deposition rate and is associated with jet/wake, and $\dot{E}_v$ is the transverse kinetic energy deposition rates and is mainly associated with lift-induced vortices. $\dot{E}_p$ is the boundary pressure-work rate associated with these flow phenomena. All three terms are interconnected through velocity/pressure exchanges, and they are gathered to form the rate of the mechanical exergy outflow.

The thermal exergy outflow:

$$\dot{\varepsilon}_{th}\coloneqq\int_{\mathcal{S}_O}\rho\delta e\left(\boldsymbol{V}\cdot\boldsymbol{n}\right)\mathrm{d}\mathcal{S}+\int_{\mathcal{S}_O}p_\infty\left(\boldsymbol{V}\cdot\boldsymbol{n}\right)\mathrm{d}\mathcal{S}-T_\infty\int_{\mathcal{S}_O}\rho\delta s\left(\boldsymbol{V}\cdot\boldsymbol{n}\right)\mathrm{d}\mathcal{S}\,. \tag{23}$$

For an ideal gas, internal energy is solely proportional to temperature. Therefore, the first term represents the rate of thermal energy outflow, the second term is the rate of enthalpy outflow, and the final term is commonly referred to as the isobaric surroundings work, generated by the irreversible work between the system and the reference atmospheric environment. The combination of these three terms represents the theoretically maximum work that can be extracted from thermal energy.

The viscous anergy:

$$\dot{\mathcal{A}}_\phi\coloneqq\int_{\mathcal{V}}\frac{T_\infty}{T}\Phi_{eff}\mathrm{d}\mathcal{V}\,, \tag{24}$$

where $\Phi_{eff}=\left(\mu+\mu_t\right)\overline{\overline{S}}$ with $\overline{\overline{S}}$ being the mean rate of strain tensor and μ_t being the eddy viscosity. $\dot{\mathcal{A}}_\phi$ is linked to viscous dissipation and turbulence, which transform any difference in kinetic energy into thermal energy. For that reason, these phenomena act toward reducing the mechanical exergy to zero by building a new homogeneous field of velocity and pressure, in which the system and its surroundings are back in mechanical equilibrium. Viscous dissipation can be expressed as a function of the square of the velocity gradient. The term is always positive, meaning exergy continuously increases, representing an irreversible process that destroys mechanical exergy.

The thermal anergy:

$$\dot{\mathcal{A}}_{\nabla T}\coloneqq\int_{\mathcal{V}}\frac{T_\infty}{T^2}k_{eff}\left(\nabla T\right)^2\mathrm{d}\mathcal{V}\,, \tag{25}$$

where $k_{eff} = c_p\left(\mu / Pr + \mu_t / Pr_t\right)$ with Pr and Pr_t being the Prandtl and turbulent Prandtl numbers, respectively. $\dot{\mathcal{A}}_{\nabla T}$ is linked to thermal mixing, which reduces the difference in temperature and therefore reduces the thermal exergy to zero. It restores thermal equilibrium between the system and the environment by establishing a uniform temperature field. Thermal mixing is a function of the square of the temperature gradient so that avoiding strong temperature variations would reduce the term. The term is also consistently positive, representing an irreversible process that destroys thermal exergy.

The wave anergy:

$$\dot{\mathcal{A}}_{\omega} \coloneqq -T_{\infty}\int_{\mathcal{S}_{\omega}} \rho\delta s\left(\boldsymbol{V}\cdot\boldsymbol{n}\right)\mathrm{d}\mathcal{S}\,. \tag{26}$$

The wave anergy converts mechanical energy into thermal energy, representing an irreversible process, it is an exergy destruction. The computation if the term relies on the definition of a shock surface $\mathcal{S}_{\omega}$ enclosing the entropy associated with the flow phenomenon.

As the distance from the object increases, the mechanical exergy $\dot{\varepsilon}_m$ and thermal exergy $\dot{\varepsilon}_{th}$ outflows are gradually dissipated due to the generation of viscous anergy $\dot{\mathcal{A}}_{\phi}$ and thermal anergy $\dot{\mathcal{A}}_{\nabla T}$, respectively. Additional losses introduced by the presence of shock wave $\dot{\mathcal{A}}_{\omega}$. In the far field of the body, the drag power DV_{∞} equals the total anergy generated. The statement was first proposed by Oswatitsch in 1956[29].

Furthermore, the relationship of Equation (21) is theoretically equivalent to the mechanical energy balance for unpowered airframes proposed by Drela[10].

2.3 Numerical Implementation

A Python-based plugin of ParaView named Epsilon developed by Aguirre et al.[30] is used to calculated each term in the exergy balance equation. After solving and validating the flow field, physical quantities at cell centers are extracted from the CFD solver using Epsilon plugin. During post-processing, the CFD results are exported to Epsilon plugin for the calculation of exergy parameters and determination of the drag coefficient.

To comprehensively evaluate all terms in Equation (21), a transverse plane perpendicular to the freestream velocity is placed in the wake. Conventional CFD meshing techniques refine near-wall regions, but such grids are inadequate for wake analysis due to significant numerical dissipation within the wake. Therefore, the wake region is specially refined to ensure losses propagate downstream without excessive dissipation. By incrementally increasing the distance between the object and the transverse plane, the Epsilon plugin writes the corresponding values of all terms in Equation (21) into the final output file.

Finally, all terms of Equation (21) are expressed in terms of power counts, abbreviated pc, such as the viscous anergy production in power counts can be expressed as

$$C\dot{\mathcal{A}}_{\phi} = \frac{\dot{\mathcal{A}}_{\phi}}{0.5\rho_{\infty}V_{\infty}^{3}A_{ref}}\,. \tag{27}$$

By doing so, their magnitudes are directly equivalent to the more traditional drag coefficients expressed in drag counts, abbreviated dc.

3. Results and Discussions

3.1 Aerodynamic Forces of CRM and BWB

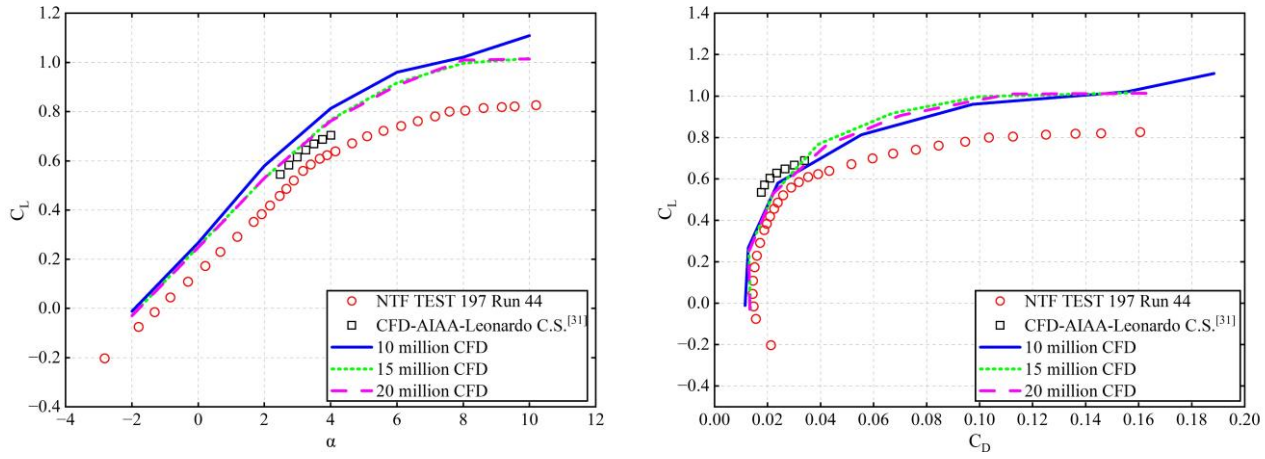
The detailed aerodynamic design of the CRM used for the fifth drag prediction workshop (DPW) was performed by teams from The Boeing Company[32]. The characteristic parameters of the reference configuration are as follows, mean aerodynamic chord (MAC) $c = 7.00m$, a reference area $S_{ref} = 382.68m^2$, an aspect ratio $AR = 9.0$, and a wingspan $b = 29.38m$. It has no vertical/horizontal stabilizers or engines.

The study uses the medium grid provided by the 5th DPW, which consists of 10 million cells with inches as the unit. An O-O grid topology is adopted, with grid points densely distributed at the wing leading edge, trailing edge, and wingtip. The far field of the grid is a hemisphere with a radius of 100 chord lengths.

In the coordinate system, the X-axis aligns with the freestream direction, the Y-axis extends spanwise outward from the view, and the Z-axis points vertically upward, following the right-hand rule. The same topology is used to refine the grid to 15 million and 20 million cells for grid convergence verification.

The freestream Mach number is $M = 0.85$, and the Reynolds number relative to the mean aerodynamic chord (MAC) is 5 million. The angle of attack varies from -2° to 10°. The CFD solver is used to numerically simulate the model, with the flow field configured as fully turbulent and employing the Spalart-Allmaras turbulence model.

The numerical results for the lift coefficient and lift-drag polar curve are compared with wind tunnel test data and the numerical results of Leonardo et al.[31], as shown in Figure 2. The near-field method is employed to compute the drag coefficient. In the linear lift region, the drag prediction is relatively accurate, while the lift is slightly higher and the moment slightly lower than the wind tunnel test results, though the trends remain consistent. At high angles of attack, notable discrepancies in lift are observed between the simulation and the wind tunnel test. The is attributed to the inability of the current turbulence model to accurately predict flow separation induced by transonic shock-boundary layer interaction. Additionally, the wind tunnel measurements are influenced by model support and wall interference effects. As the grid resolution increases, the deviation from experimental results decreases, thereby confirming the reliability of both the grid and the numerical simulation methodology.



(a) Lift coefficient (b) Lift-drag polar curve

Figure 2- Comparisons of the force coefficients of CFD and wind-tunnel test for CRM at $\mathrm{Re} = 5 \times 10^6$, $M = 0.85$

The CFD simulation and drag composition analysis are conducted on the high-speed wind-tunnel test model of a clean BWB configuration civil aircraft designed by the Northwestern Polytechnical University team. The characteristic parameters of the configuration are as follows: $MAC = 0.367m$, full-model reference area $S_{ref} = 0.1805m^2$, and wingspan $b = 0.9m$. The schematic diagram of the BWB configuration is shown in Figure 3.

The computational mesh contains 10 million cells, with units in meters. The mesh topology is of O-H type, with refined clustering at the wing leading edge, trailing edge, and wingtip. The coordinate system follows the right-hand rule: the X-axis aligns with the freestream direction, the Y-axis points vertically upward, and the Z-axis extends outward along the spanwise direction. The same topology is used to refine the grid to 15 million and 20 million cells for grid convergence verification.

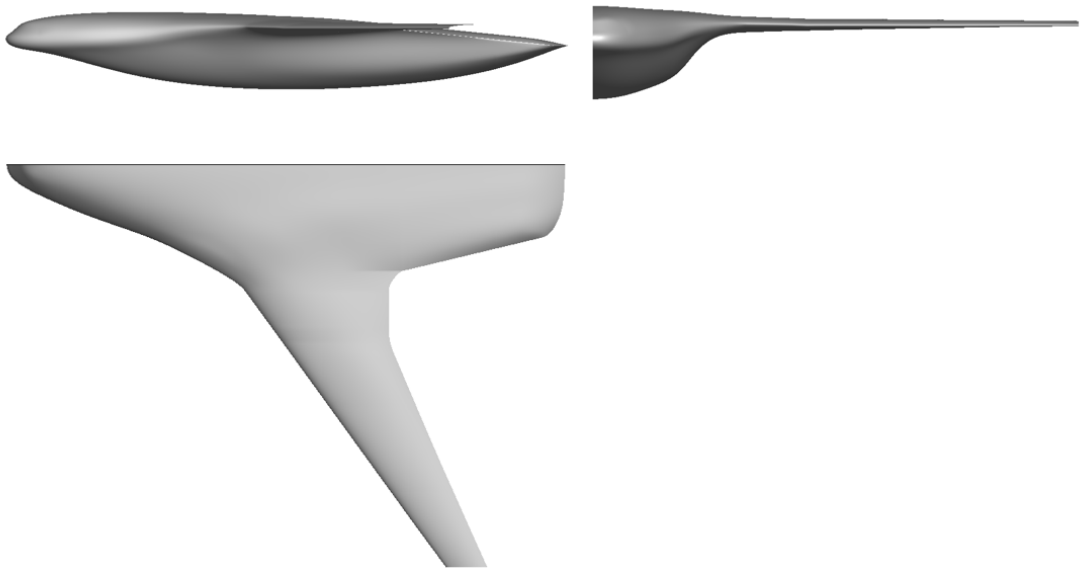
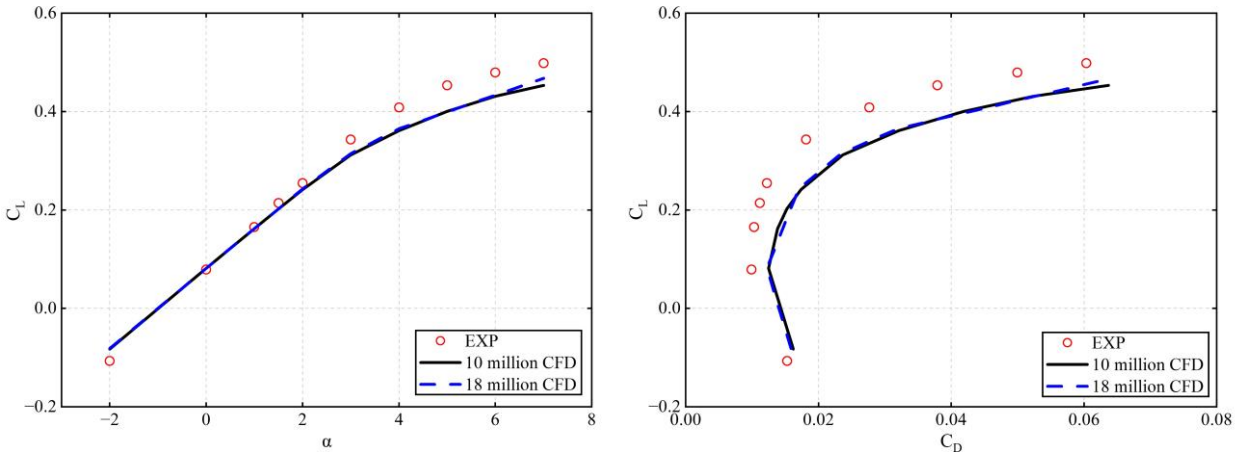


Figure 3- Schematic of the BWB configuration

The freestream Mach number is $Ma = 0.85$, and the Reynolds number relative to the mean aerodynamic chord is 6.35 million. The target-lift algorithm is applied to adjust the angle of attack such that the lift coefficient meets the design-point requirement across all grid levels, with the resulting angle of attack falling within approximately 2°. The numerical results for lift coefficient, and lift-drag polar curve are compared with wind tunnel test data as shown in Figure 4.



(a) Lift coefficient (b) Lift-drag polar curve

Figure 4- Comparisons of the force coefficients of CFD and wind-tunnel test for BWB at $\mathrm{Re} = 6.35\times10^6$, $M = 0.85$

3.2 Comparisons of Three Drag-Prediction Methods

To validate the reliability of the exergy method, the drag prediction results obtained using the exergy method are compared with those from the near-field and far-field methods. For more intuitive results, the difference ratio is provided:

$$error_{\varepsilon,nf} = \left| \frac{CD_\varepsilon - CD_{nf}}{CD_{nf}} \right| \times 100\% , \tag{28}$$

$$error_{\varepsilon,ff} = \left| \frac{CD_\varepsilon - CD_{ff}}{CD_{ff}} \right| \times 100\% . \tag{29}$$

The computational results of three drag-prediction methods are given in Table 1 for CRM and BWB. For CRM, the drag decomposition is performed at design lift coefficient of 0.5 corresponds to an angle of attack of 2°. The transverse planes for both aircrafts are located 2 mean aerodynamic chords downstream in the wake.

Overall, under cruise conditions, the BWB experiences a lower total drag due to its larger reference area. For the CRM, induced drag accounts for 63% of the total drag, whereas for the BWB configuration, induced drag constitutes only 24% of the total drag. The indicates that the BWB configuration effectively reduces induced drag and mitigates the energy loss associated with vortex dissipation. Pressure drag constitutes 68.7% of the total drag for the CRM, whereas it accounts for only 48.9% for the BWB. This reduction stems from the BWB's complete elimination of the non-lifting tubular fuselage typical of conventional configurations. By seamlessly blending the fuselage and wing into a continuous, aerodynamically integrated surface, nearly the entire airframe contributes to lift generation, thereby substantially optimizing the pressure distribution. BWB not only avoids the severe flow interference and separation that occur at the junction of a conventional fuselage and wing but also results in a smoother flow from the nose to the tail of the aircraft. Consequently, both the fore-aft pressure difference and the adverse pressure gradient are significantly reduced, leading to a fundamental decrease in pressure drag. Additionally, the friction drag, viscous drag, and wave drag coefficients show comparable values between the CRM and BWB.

The results obtained from the three drag-prediction methods demonstrate the reliability of the exergy-based method, confirming its suitability for subsequent flow-field analysis aimed at revealing the physical mechanisms of energy conversion.

Table 1 Comparison of Results from Three Drag-prediction Methods

Model	Near-field method		Far-field drag method			Exergy-based method					Difference Ratio	
	CD_{nf}		CD_{ff}			CD_{ε}					$error_{\varepsilon,nf}$	$error_{\varepsilon,ff}$
	CD_f	CD_p	CD_v	CD_i	CD_w	$C\dot{\varepsilon}_m$	$C\dot{\varepsilon}_{th}$	$C\dot{\mathcal{A}}_{\phi}$	$C\dot{\mathcal{A}}_{\nabla T}$	$C\dot{\mathcal{A}}_w$		
CRM	221.8		220.7			222.2					0.18%	0.68%
	69.2	152.5	78.3	139.0	3.4	130.7	6.1	75.9	6.2	3.3		
BWB	121.6		120.2			121.5					0.06%	1.08%
	62.1	59.5	87.8	28.9	3.5	32.4	1.3	78.6	5.8	3.4		

Table 2 presents the power-counting results of all terms in equation (21) for both models.

Table 2- Exergy-based drag power breakdown

Model	$C\dot{\varepsilon}_m$	$C\dot{\varepsilon}_p$	$C\dot{\varepsilon}_u$	$C\dot{\varepsilon}_v$	$C\dot{\varepsilon}_{th}$	$C\dot{\mathcal{A}}_{\phi}$	$C\dot{\mathcal{A}}_{\nabla T}$	$C\dot{\mathcal{A}}_w$	CD_{ε}
CRM	130.7	-15.5	10.3	136.0	6.1	75.9	6.2	3.3	222.2
BWB	32.4	-0.83	4.7	28.6	1.3	78.6	5.8	3.4	121.5

Regarding exergy outflows, the magnitude of mechanical exergy is larger than that of thermal exergy and is comparable to the lateral kinetic energy of the lift-induced vortices.

In terms of anergy production, wave anergy agrees well with the wave drag predicted by the far-field method, and the magnitude of viscous dissipation is one order of magnitude higher than that of thermal dissipation.

To conclude aerodynamic assessment from an exergy/anergy standpoint. For CRM, mechanical aspects represent about 93% of the total anergy that the airplane involves. Then, thermal aspects are second-order contributors to the drag, around 5%. The wave anergy accounts for the remaining 2%. The approach also highlights that only 38% of the total anergy has been produced at a distance of 2 MAC downstream of the airplane. In other words, there is a large recoverable work potential present in the wake of the airplane. For BWB, mechanical aspects represent about 91.4% of the total anergy that the airplane involves. Then, thermal aspects are second-order contributors to the drag, around 5.8%. The wave anergy accounts for the remaining 2.8%. 72% of the total anergy has been produced

at a distance of 2 MAC downstream of the airplane.

3.3 Drag transformation along streamwise direction

3.3.1 CRM

A qualitative and quantitative flow analysis is made on the 20 million mesh, first in terms of exergy outflows and then in terms of anergy generation.

The evolution of each component of the mechanical exergy along the flow direction of the aircraft is shown in Figure 5, i.e., $\dot{\varepsilon}_m = \dot{E}_u + \dot{E}_v + \dot{E}_p$.

The disturbance induced by the aircraft to the incoming flow is clearly observed within $0 < x/c < 1$, especially it forces the flow to get round the nose, leading to an increase in its transverse kinetic energy $\dot{E}_v$. At about $x/c = 2$, all perturbations have decayed. Then the region of most pronounced flow variation appears near the wing: due to the reduction in static pressure, $p - p_\infty$ attains a relatively large negative value, accelerating the incoming flow and causing the pressure boundary-work rate $\dot{E}_p$ to exhibit a significant negative value. The acceleration also enhances the streamwise kinetic energy $\dot{E}_u$.

The transverse kinetic energy $\dot{E}_v$ shows a relatively steady growth ahead of the wingtip and remains nearly constant afterward. In the immediate downstream region of the wing, the streamwise kinetic energy $\dot{E}_u$ and the pressure boundary-work rate $\dot{E}_p$ are essentially in balance, so that the mechanical exergy $\dot{\varepsilon}_m$ consists only of the transverse kinetic energy component, associated with the lift-induced vortices.

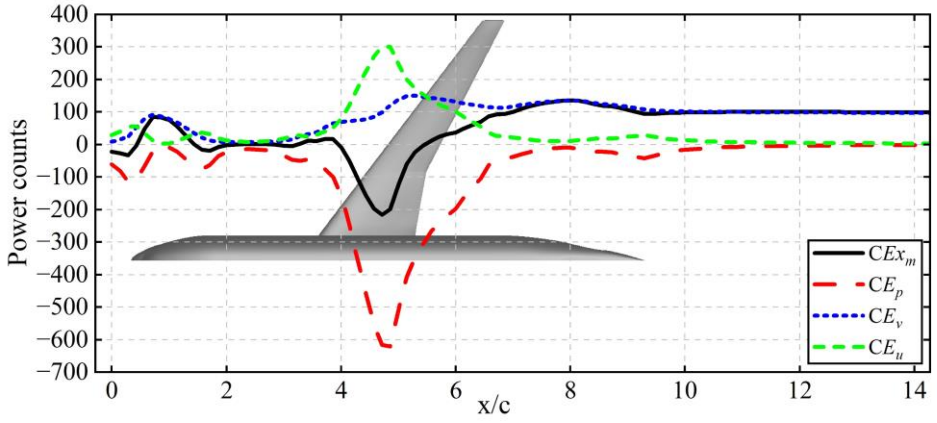


Figure 5-Mechanical exergy distribution over the body

One key function of exergy analysis is to identify improvable aspects in fluid flow. The subject of the study generates perturbations in velocity, pressure, and temperature, which, in order to satisfy Second Law requirements, these perturbations must be dissipated. Before these deviations from the reference state are suppressed, they represent potential improvement opportunities due to their exploitable value. The exergy-waste coefficient (EWC) can be introduced to quantify the relative amount of exergy loss:

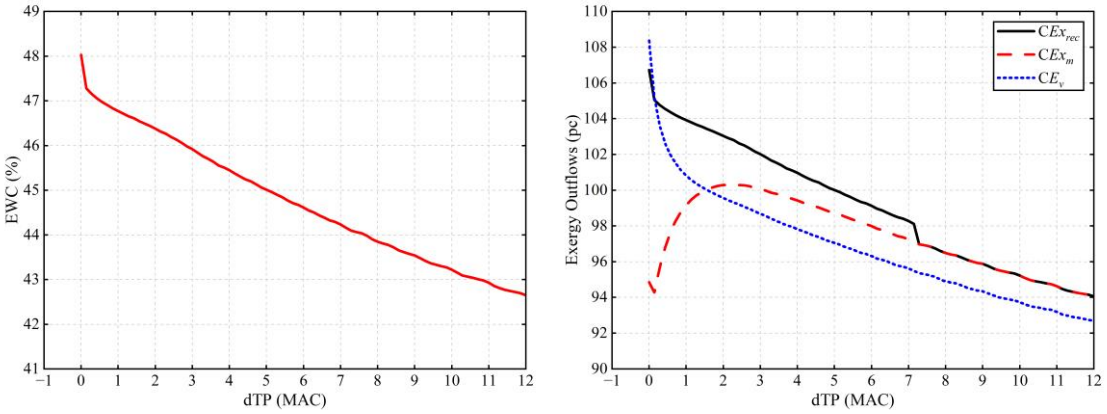
$$EWC = \frac{\dot{\varepsilon}_{rec}}{\dot{\varepsilon}_{rec} + \dot{\mathcal{A}}_{tot}} = \frac{\dot{\varepsilon}_m + \dot{\varepsilon}_{th}}{DV_\infty}, \tag{30}$$

where coverable exergy $\dot{\varepsilon}_{rec}$ is made up of a mechanical part $\dot{\varepsilon}_m$ and a thermal part $\dot{\varepsilon}_{th}$.

Figure 6a illustrates the variation of the coefficient over the downstream range from 0 to 12 mean aerodynamic chords behind the aircraft. At a distance of 11 mean aerodynamic chords, EWC =43%. The result is derived from flow analysis at such a large distance downstream of the fuselage and involves uncertainty. Where dTP is defined as the distance from the downstream traverse plane to the

aircraft tail, normalized by the MAC.

From Figure 6b, it can be observed that recoverable exergy exists primarily in mechanical form, whereas thermal exergy outflow dissipates rapidly. This behavior stems from the presence of lift-induced vortices in the far field, whose associated transverse kinetic energy constitutes the dominant contribution from the aircraft. This potential can be partially recovered via turbines mounted at the wingtips[33]. Furthermore, formation flight can also exploit the transverse kinetic energy present in the aircraft's far-field wake[34].



(a) Exergy-waste coefficient (b) Decomposition of the recoverable exergy

Figure 6- Recoverable exergy in the wake

The anergy field is depicted in Figure 7 by the shock surfaces are shown in red, while the iso-surfaces of thermal anergy and viscous anergy are presented in blue and green.

Iso-surfaces corresponding to wake dissipation extend several body lengths downstream of the aircraft, persisting to the grid boundary. The observation holds on the finest grid. However, on coarser grids, these iso-surfaces decay more rapidly as numerical dissipation exceeds physical dissipation. Thermal anergy is primarily generated in the fuselage wake, whereas viscous anergy is distinctly associated with the lift-induced vortices. Furthermore, the wing region is magnified to illustrate shock-wave formation. For clarity regarding their distribution over the wing, a front view of the configuration is presented in the right-hand figure. Within the airframe region, shock waves are minimally generated and occur primarily on the upper wing surface.

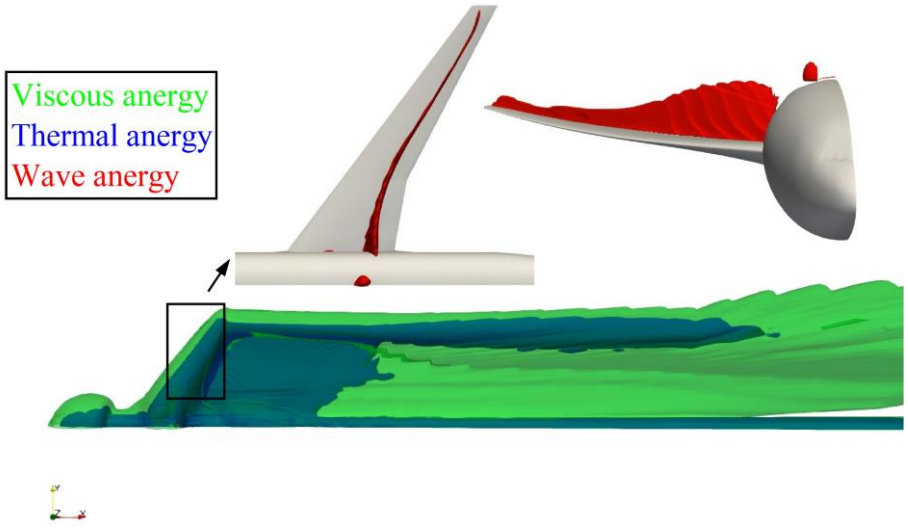
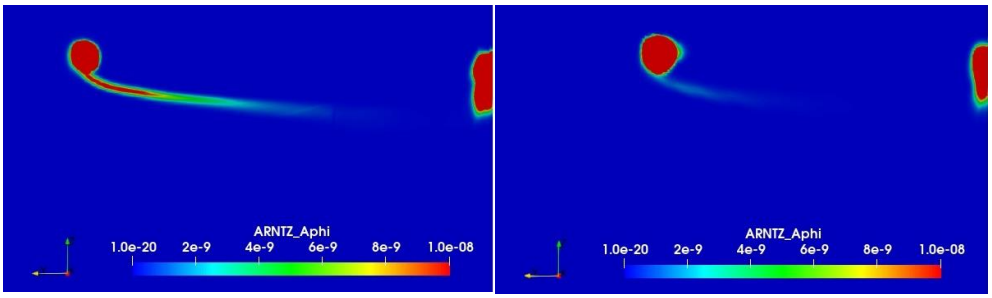


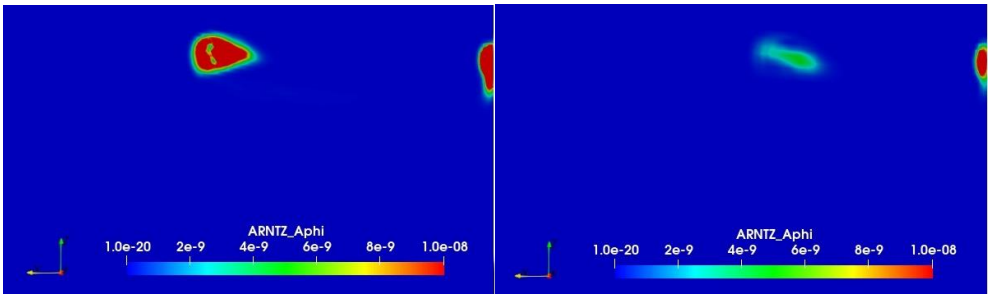
Figure 7- Thermal and viscous anergy isosurfaces with shock wave surface

Figure 8 and Figure 9 depict the evolution of viscous and thermal anergy as transverse planes are moved downstream along the wake. In Figure 8, the viscous anergy associated with the wingtip vortices diminishes in the far field as the vortices gradually dissipate, whereas viscous anergy continues to be generated in the fuselage wake region. Compared with viscous anergy, thermal anergy

decays more rapidly in the far field. The origin is located at the aircraft nose.

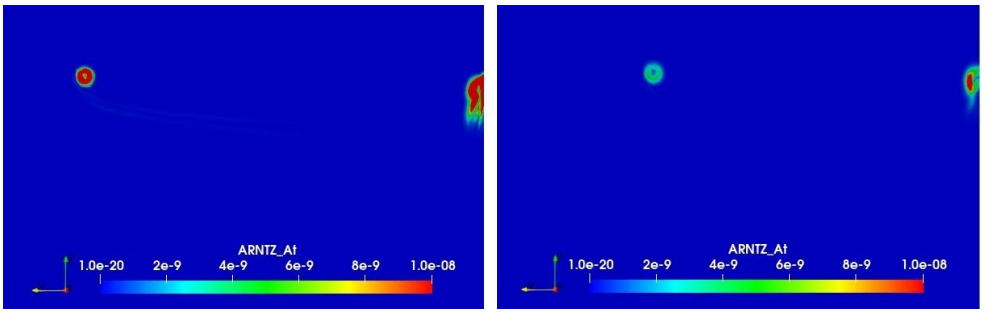


(a) x/c=10 (b) x/c=12

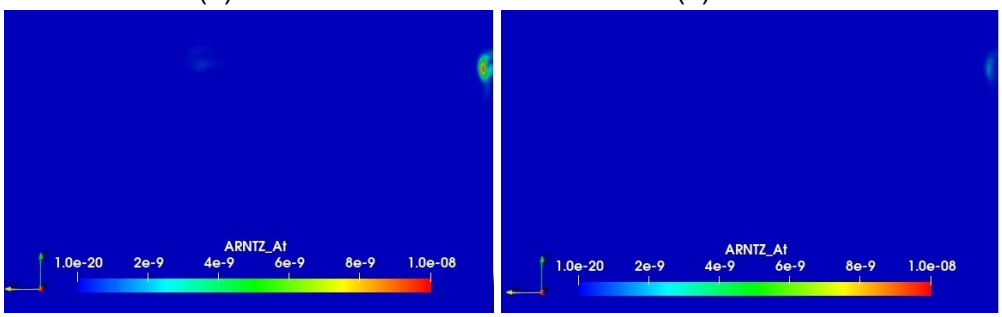


(c) x/c=14 (d) x/c=19

Figure 8- The viscous anergy increases as the transverse planes are positioned farther downstream from x/c=10 to x/c=19



(a) x/c=10 (b) x/c=12



(c) x/c=14 (d) x= x/c=19

Figure 9- The thermal anergy increases as the transverse planes are positioned farther downstream from x/c=10 to x/c=19

Quantitatively, Figure 10 presents the streamwise distribution of anergy generation rate. In terms of streamwise distribution, the region immediately downstream of the fuselage corresponds to the dissipation zone caused by fuselage-induced disturbances. Subsequently, the wing becomes the dominant source of anergy generation. The generation rates of all dissipation phenomena decrease rapidly in the wake. Viscous anergy destruction predominates, which aligns with the qualitative assessment by Alabi et al.[35] for a Boeing B747-200 under cruise conditions.

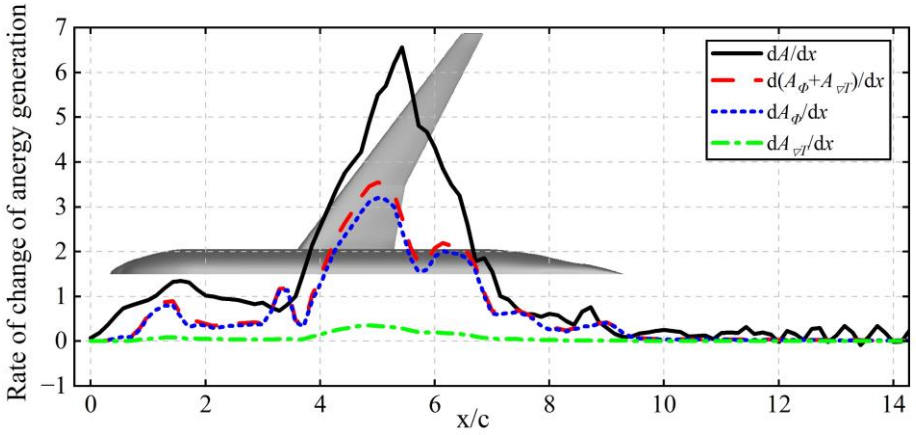


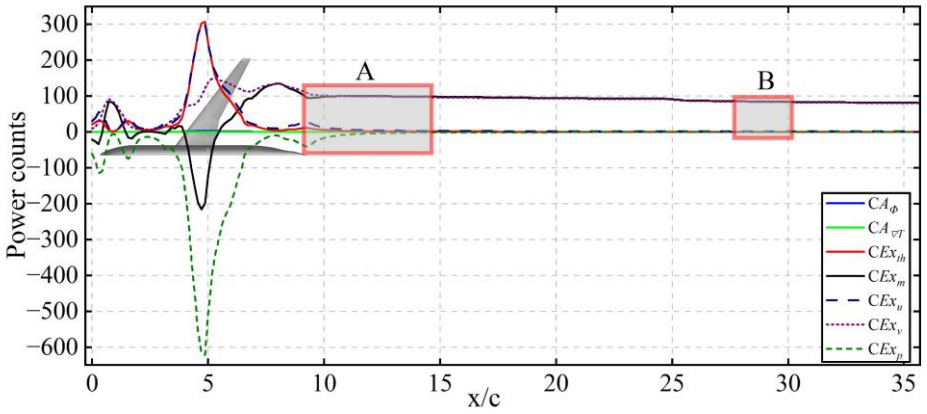
Figure 10- The streamwise distribution of anergy generation rate

To investigate the influence of different transverse planes along the wake direction on individual exergy components, Figure 11a presents the streamwise evolution of each exergy component in the flow field. All components of exergy and anergy decrease rapidly in the wake region behind the fuselage.

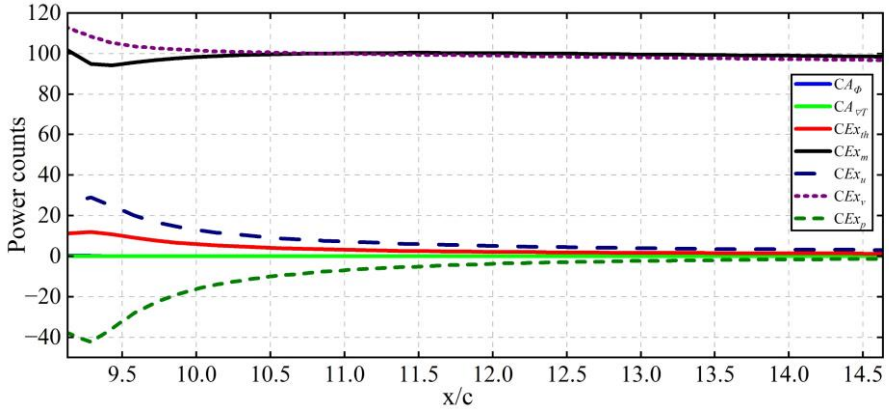
Figure 11b provides a close-up view at a distance of 5 mean aerodynamic chords downstream of the fuselage. Given that the fuselage ends at $x/c \approx 9$, the flow velocity gradually recovers to the freestream value behind the body, causing the streamwise kinetic energy to decrease. As the static pressure in the wake rises toward the freestream static pressure, the pressure boundary-work rate increases. With increasing distance from the body, the vortex wake dissipates significantly, leading to a reduction in transverse kinetic energy. Overall, mechanical exergy exhibits an increasing trend. Thermal exergy, primarily associated with temperature variations, decreases as the temperature rise induced by flow acceleration gradually diminishes until the freestream temperature is recovered farther downstream.

Viscous anergy, linked to the conversion of kinetic energy into thermal energy, continuously diminishes mechanical energy by driving the system toward mechanical equilibrium through the homogenization of velocity and pressure fields, representing the dissipation of mechanical energy via irreversible processes. Thermal anergy characterizes thermal mixing effects, decreasing toward zero as temperature differences are eliminated, thereby restoring thermal equilibrium between the system and the environment. Within the control volume, both anergy components increase as the transverse plane moves farther downstream, indicating that the recoverable portion of energy in the flow is progressively transformed into irrecoverable loss. Although variations in each component are more pronounced in the near-wake region, exergy and anergy remain in balance at every transverse plane. Consequently, their sum changes only slightly, differing by approximately 5pc between the 1 MAC and 2 MAC locations.

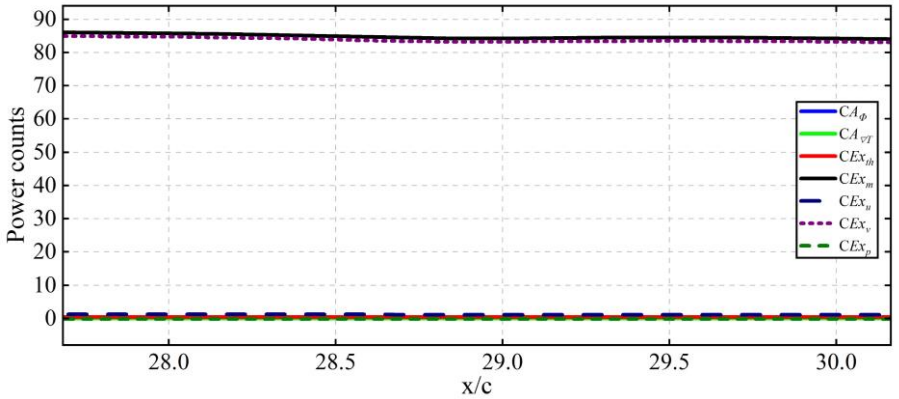
When the transverse plane is placed sufficiently far downstream, as shown in Figure 11c, the pressure boundary-work rate, streamwise kinetic energy, and thermal exergy all asymptotically approach zero with minimal variation, leaving mechanical exergy solely composed of the transverse kinetic energy component. At the stage, mechanical equilibrium between the system and the environment is effectively restored.



(a) Overall distribution



(b) Close-up of Region A



(c) Close-up of Region B

Figure 11- Streamwise distribution of exergy and anergy components in the wake

3.3.2 BWB

For the BWB configuration, as depicted in Figure 12, the aircraft induces relatively minor disturbances in the incoming flow. Consequently, the components related to mechanical exergy do not exhibit significant fluctuations near the nose region. However, the mechanical-exergy terms still undergo pronounced variations in the wing region. Toward the rear of the airframe, the streamwise kinetic energy decreases rapidly, while the pressure boundary-work rate increases, leading to an overall rise in mechanical exergy. The transverse kinetic energy associated with induced drag shows no marked overall change in magnitude. Ultimately, the mechanical exergy remains composed solely of the transverse kinetic energy component.

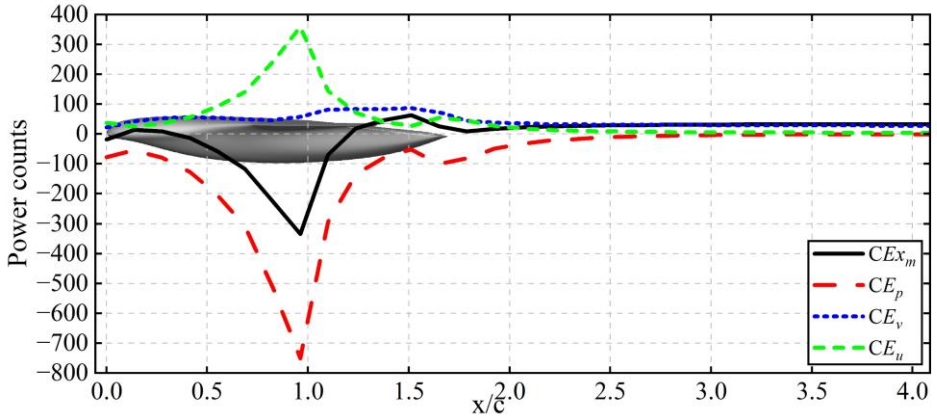
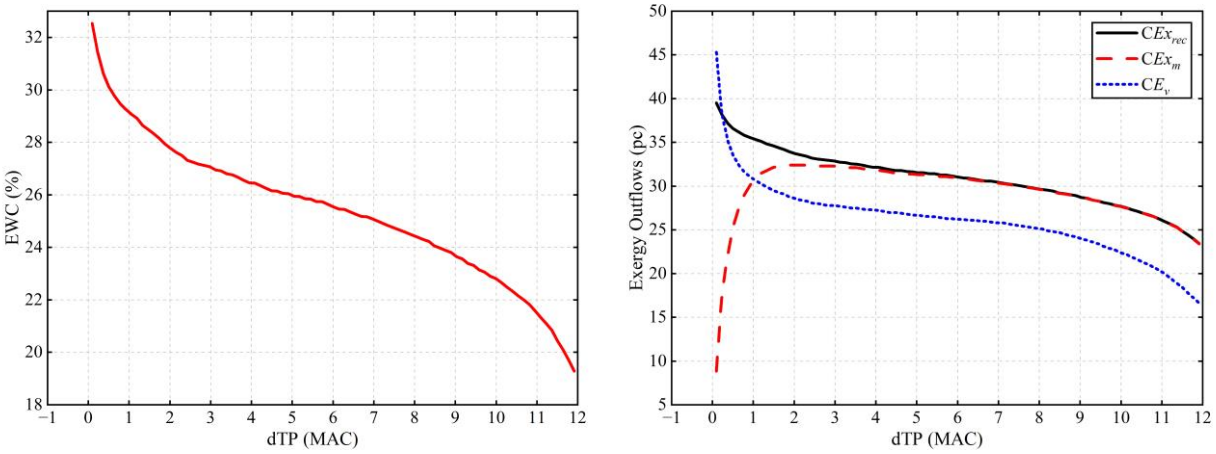


Figure 12- Mechanical exergy distribution over the body

The variation of the exergy-waste coefficient (EWC) at approximately 12 mean aerodynamic chords downstream of the aircraft are shown in Figure 13a. At 11 mean aerodynamic chords, the EWC reaches 21.3%. In contrast, the CRM exhibits an exergy-waste coefficient of 43% at a downstream distance of 11 mean aerodynamic chords, indicating that the BWB configuration achieves higher energy-utilization efficiency than the conventional layout.

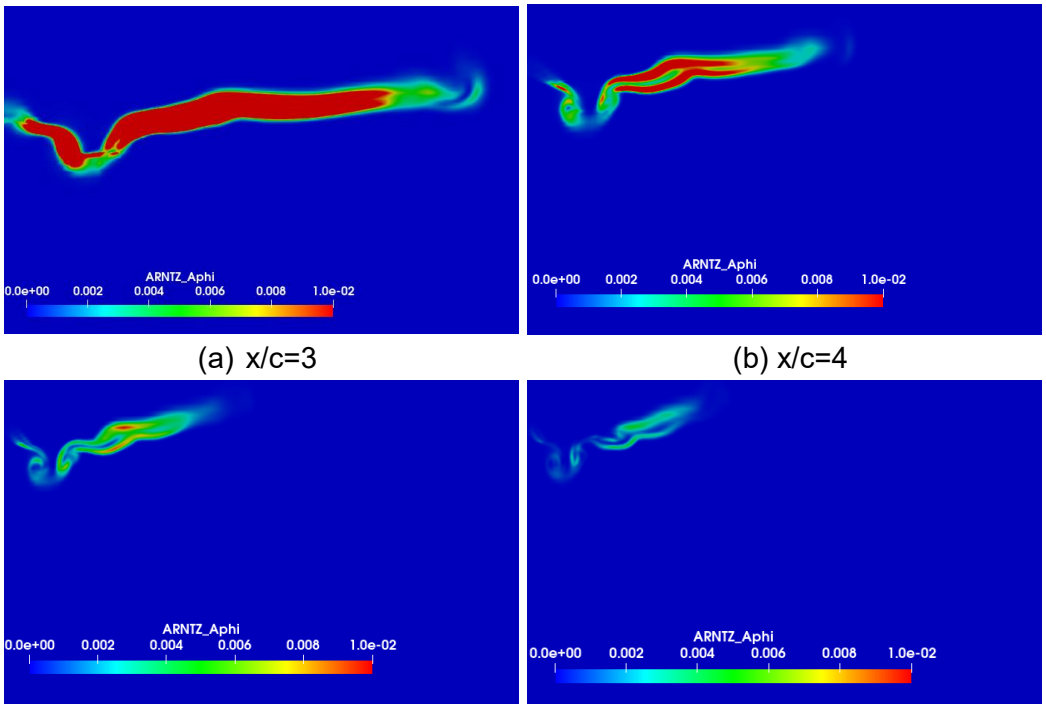
As seen in Figure 13b, the recoverable exergy in the BWB configuration remains predominantly in mechanical form, while the outflow of thermal exergy dissipates rapidly. This is attributed to the presence of lift-induced vortices in the far field, whose associated transverse kinetic energy constitutes a primary contribution generated by the aircraft. Since the BWB configuration produces lower induced drag, its transverse kinetic energy is correspondingly smaller than that of the CRM.



(a) Exergy-waste coefficient (b) Decomposition of the recoverable exergy

Figure 13- Recoverable exergy in the wake

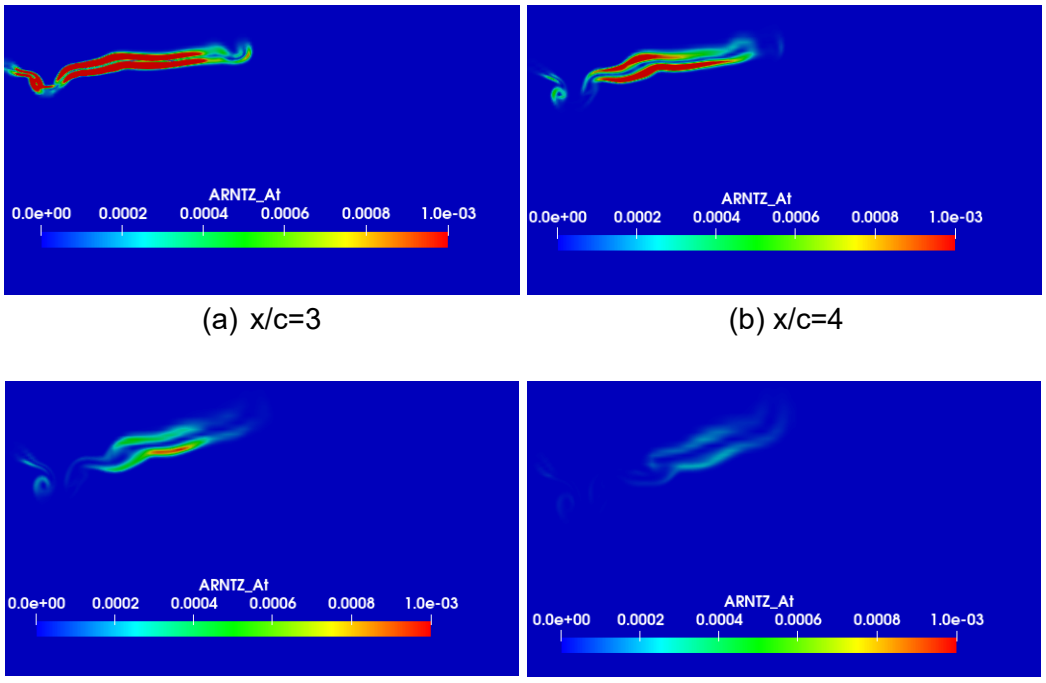
Figure 14 and Figure 15 depict the evolution of viscous and thermal anergy as transverse planes are moved downstream along the wake. In contrast to the CRM, viscous anergy in the BWB configuration does not arise significantly from vortex formation. Compared with viscous anergy, thermal anergy decays more rapidly in the far field. The origin is located at the aircraft nose.



(a) x/c=3 (b) x/c=4

(c) x/c=5 (d) x/c=7

Figure 14- The viscous anergy increases as the transverse planes are positioned farther downstream from x/c=3 to x/c=7



(a) x/c=3 (b) x/c=4

(c) x/c=5 (d) x/c=7

Figure 15- The thermal anergy increases as the transverse planes are positioned farther downstream from x/c=3 to x/c=7

Quantitatively, Figure 16 presents the streamwise distribution of anergy generation rate. From the streamwise distribution, the dissipation caused by flow disturbance near the nose of the BWB configuration is significantly smaller than that of the CRM, with almost no anergy generated around the nose region. Subsequently, the wing becomes the dominant source of anergy generation. The production rates of all dissipation phenomena decrease rapidly in the wake. Among these, viscous anergy destruction is predominant.

Visualizing the flow field from an anergy perspective enables aircraft designers to locate loss regions within the flow. In the way, potential areas for improvement can be identified, and the impact of configuration modifications can be intuitively evaluated. For BWB configurations, aerodynamic losses cannot be clearly separated into viscous, wave, and lift-induced drag, as drag itself is difficult to define explicitly. The exergy method by Arntz offers an advantage by providing a global accounting and phenomenological decomposition.

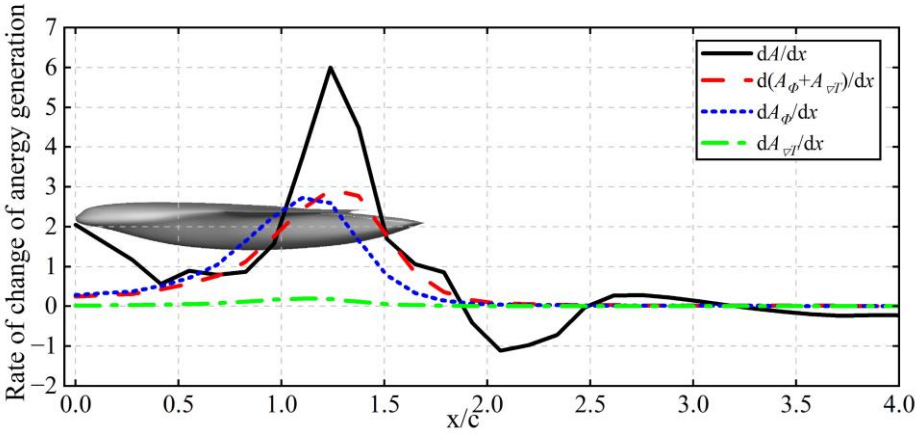


Figure 16- The streamwise distribution of anergy generation rate

4. Conclusions

To analyze the origins of different drag components and the physical mechanisms governing their mutual conversion, the study applies Arntz's exergy-based method to compare the NASA Common Research Model (CRM) and a Blended Wing Body (BWB) configuration civil aircraft under transonic cruise conditions. The main findings are summarized as follows.

Overall, within the wake region, the outflow of mechanical exergy exceeds that of thermal exergy and is comparable in magnitude to the lateral kinetic energy associated with lift-induced vortices. Regarding anergy production, wave anergy correlates closely with the wave drag predicted by the far-field method, while viscous dissipation is an order of magnitude greater than thermal dissipation. Under transonic cruise conditions, the total drag of the BWB configuration is lower than that of the CRM. Induced drag accounts for 63% of the total drag for the CRM, but only 24% for the BWB configuration. This indicates that the BWB design effectively reduces induced drag during transonic cruise and offers a distinct drag reduction advantage over conventional configurations.

Regarding the drag decomposition, pressure drag accounts for 68.7% of the total drag for the CRM, but only 48.9% for the BWB. This reduction is primarily attributable to the BWB's complete elimination of the non-lifting tube fuselage of conventional configurations. By seamlessly blending the fuselage and wing into a continuous, aerodynamically integrated surface, nearly the entire airframe contributes to lift generation, thereby substantially optimizing the pressure distribution. The BWB configuration not only avoids the severe flow interference and separation typically occurring at the junction of a conventional fuselage and wing but also promotes smoother flow from the nose to the tail of the aircraft. As a result, both the fore-aft pressure difference and the adverse pressure gradient are significantly reduced, leading to a fundamental decrease in pressure drag. In contrast, the friction drag, viscous drag, and wave drag coefficients show comparable values between the CRM and BWB configurations.

As the flow passes over the aircraft, the exergy and anergy near the nose of the CRM initially increase and then decrease due to local flow disturbances. This behavior is not observed in the BWB configuration, where notable variations in exergy and anergy occur only in the wing region. In the aircraft wake, the CRM exhibits an exergy waste coefficient of 43% associated with lift-induced vortices, whereas the BWB configuration shows a value of only 21.3%. This result indicates that the BWB configuration achieves significantly higher energy utilization efficiency compared to the conventional layout.

Downstream of the fuselage, the decrease in flow velocity and temperature, along with the increase in static pressure, leads to a reduction in streamwise kinetic energy and thermal exergy, while the

pressure boundary work rate increases. The transverse kinetic energy associated with vortical motion also decreases due to vortex dissipation. Meanwhile, viscous anergy converts kinetic energy into thermal energy by driving the system toward mechanical equilibrium through homogenization of the velocity and pressure fields. This process continuously consumes mechanical energy, thereby quantifying the irreversible dissipation of mechanical work. Thermal anergy characterizes thermal mixing and approaches zero as temperature differences diminish, which restores thermal equilibrium between the system and the environment and marks the dissipation of thermal exergy. Within the control volume, anergy increases as the transverse plane moves downstream, indicating that the recoverable portion of the flow energy is progressively transformed into irrecoverable loss as the wake develops.

5. Contact Author Email Address

Corresponding author: zhenlichen@nwpu.edu.cn

6. Copyright Statement

The authors confirm that they, and/or their company or organization, hold copyright on all of the original material included in the paper. The authors also confirm that they have obtained permission, from the copyright holder of any third party material included in the paper, to publish it as part of their paper. The authors confirm that they give permission, or have obtained permission from the copyright holder of the paper, for the publication and distribution of the paper as part of the ICAS proceedings or as individual off-prints from the proceedings.

References

[1] Airbus. Airbus Global Market Forecast 2025-2044. 2025.

[2] McMullen B. Boeing Commercial Market Outlook, 2025-2044. 2025.

[3] Gohardani A S, Doulgeris G, and Singh R. Challenges of Future Aircraft Propulsion: A Review of Distributed Propulsion Technology and Its Potential Application for the All Electric Commercial Aircraft. Progress in Aerospace Sciences, Vol. 47, No. 5, 2011, pp. 369–391.

[4] Ashcraft S W, Padron A S, and Pascioni K A. Review of Propulsion Technologies for N+3 Subsonic Vehicle Concepts. NASA TM-2011-217239, 2011.

[5] van der Vooren J, and Destarac D. Drag/Thrust Analysis of Jet Propelled Transonic Transport Aircraft: Definition of Physical Drag Components. Aerospace Science and Technology, Vol. 8, No. 6, 2004, pp. 545–556.

[6] Destarac D. Far-Field / Near-Field Drag Balance and Applications of Drag Extraction in CFD. CFD-Based Aircraft Drag Prediction and Reduction, VKI Lecture Series 2003, National Institute of Aerospace, Hampton, VA, 2003.

[7] Bailly D, Petropoulos I, and Wervaecke C, et al. An Overview of ONERA Research Activities Related to Drag Analysis and Breakdown. AIAA Aviation 2021 Forum, AIAA Paper 2021-2551, 2021.

[8] Wu J Z, Roach R L., and Lo C F, et al. Aerodynamic diagnostics and design based on boundary vorticity dynamics. 1999, *AIAA Paper* 99-3103.

[9] Wu J Z, Pan Z L, Lu X Y. Unsteady fluid-dynamic force solely in terms of control-surface integral. 2005, Phys. Fluids 17, 098102.

[10] Drela M. Power Balance in Aerodynamic Flows. AIAA Journal, Vol. 47, No. 7, 2009, pp. 1761–1771.

[11] Sanders D S, and Laskaridis P. Full-Aircraft Energy-Based Force Decomposition Applied to Boundary-Layer Ingestion. AIAA Journal, Vol. 58, No. 10, 2020, pp. 4357–4373.

[12] Arntz A, Atinaul O, and Merlen A. Exergy-Based Formulation for Aircraft Aero propulsive Performance Assessment: Theoretical Development. AIAA Journal, Vol. 53, No. 6, 2015, pp. 1627–1639.

[13] Çengel Y A, and Boles M A. *Thermodynamics: An Engineering Approach*. 8th ed., McGraw–Hill, New York, 2015, Chap. 8.

[14] Rant Z. Exergie, ein Neues Wort für Technische Arbeitsfähigkeit. Forschung im Ingenieurwesen, Vol. 22, No. 1, 1956, pp. 36–37.

[15] Moran M J Sciubba E. Exergy Analysis: Principles and Practice. Journal of Engineering for Gas Turbines and Power, Vol. 116, No. 2, 1994, pp. 285–290.

[16] Moorhouse D, Camberos J, and Suchomel C. Entropy and Exergy Balance Equations for MHD Flow with Application to Hypersonic Vehicle Analysis and Design," 33rd Plasmadynamics and Lasers Conference, AIAA Paper 2002-2183, 2002.

[17] Camberos J. On the Construction of Exergy Balance Equations for Availability Analysis. 8th AIAA/ASME Joint Thermophysics and Heat Transfer Conference, AIAA Paper 2002-2880, 2002.

[18] Arntz A. Civil Aircraft Aero-Thermo-Propulsive Performance Assessment by an Exergy Analysis of High-Fidelity CFD-RANS Flow Solutions. Ph.D. Thesis, Lille 1 University–Sciences and Technologies, Lille, France, 2014.

[19] Petropoulos I, Wervaecke C, and Bailly D, et al. Numerical Investigations of the Exergy Balance Method for Aerodynamic Performance Evaluation. AIAA Aviation 2019 Forum, AIAA Paper 2019-2926, 2019.

[20] Aguirre M Á, and Duplaa S. Exergetic Drag Characteristic Curves. AIAA Journal, Vol. 57, No. 7, 2019, pp. 2746–2757.

[21] Aguirre M Á, Duplaa S, and Carbonneau X, et al. Velocity Decomposition Method for Exergy-Based Drag Prediction. AIAA Journal, Vol. 58, No. 11, 2020, pp. 4686–4701.

[22] Aguirre M Á. Exergy Analysis of Innovative Aircraft with Aero propulsive Coupling. Ph.D. Thesis, ISAE-Supaero, 2022.

[23] Berhouni I, Bailly D, and Petropoulos I. On the Definition of Exergy in the Field of Aerodynamics. AIAA Journal, Vol. 61, No. 10, October 2023.

[24] Berhouni I, Bailly D, and Petropoulos I. Exergy Balance Extension to Rotating Reference Frames: Application to a Propeller Configuration. AIAA Journal Vol. 61 No. 4 (2023): pp. 1790–1806.

[25] Ilias Petropoulos, Didier Bailly, and Ily`es Berhouni. Development of numerical accuracy indicators for the far-field exergy balance method. In AIAA Aviation Forum 2023, Paper 2023-3389.

[26] Betz A. Ein Verfahren zur Direkten Ermittlung des Profilwiderstandes. *Zeitschrift für Flugtechnik un Motorluftschiffahrt,* Vol. 16, 1925, pp. 42–44.

[27] Meheut M. Evaluation des Composantes Phénoménologiques de la Trainée d'un Avion à Partir des Résultats Expérimentaux. Thèse ONERA, 2006.

[28] Kusunose A. Wake Integration Method for Airplane Drag Prediction. Tohoku Univ. Press, Sendai, Japan, 2005.

[29] Oswatitsch K. *Gas Dynamics*. Academic Press, New York, 1956, Chaps. 4, 11.

[30] Aguirre M, Duplaa S. Epsilon: An Open Source Tool for Exergy-Based Aerodynamic Analysis. Aerospace Europe Conference, 25-28 February 2020, Bordeaux, France.

[31] Leonardo C S, de Souza, R F. Grid assessment using the NASA common research model (CRM) wind tunnel data. In Proceedings of the 51st AIAA Aerospace Sciences Meeting including the New Horizons Forum and Aerospace Exposition, Grapevine, TX, USA, 7–10 January 2013.

[32] Vassberg J C, DeHaan M A, and Rivers, S. M. Development of a Common Research Model for Applied CFD Validation Studies. 26th AIAA Applied Aerodynamics Conference, AIAA Paper 2008-6919, 2008.

[33] Patterson J C, Jr, and Flechner S G. Exploratory Wind-Tunnel Investigation of a Wingtip-Mounted Vortex Turbine for Vortex Energy Recovery. NASA Technical Paper 2468, 1985.

[34] Vachon M J, Ray R J, and Walsh K R, et al. F/A-18 Performance Benefits Measured During the Autonomous Formation Flight Project. NASA TM-2003-210734, 2003.

[35] Alabi K, Ladeinde F, and von Spakovsky, et al. The Use of the 2nd Law as a Potential Design Tool for Aircraft Air Frame Subsystems. International Journal of Thermodynamics, Vol. 9, No. 4, 2006, pp. 1–14.